The hadron calorimeter of EAS-TOP: operation, calibration and resolution

The EAS-TOP Collaboration

R. Adinolfi Falcone[a], M. Aglietta[b,c], B. Alessandro[c], P. Antonioli[d], F. Arneodo[a,e],
L. Bergamasco[c,f], M. Bertaina[c,f], R. Bertoni[b,c], A. Campos Fauth[g], C. Castagnoli[b,f],
A. Castellina[b,c,*], A. Chiavassa[c,f], G. Cini Castagnoli[c,f], B. D'Ettorre Piazzoli[h],
G. Di Sciascio[h], W. Fulgione[b,c], P. Galeotti[c,f], P.L. Ghia[b,c], A. Giuliano[b,c],
M. Iacovacci[h], G. Mannocchi[b,c], C. Morello[b,c], G. Navarra[c,f], H. Nogima[g],
L. Riccati[c], O. Saavedra[c,f], E. Tatananni[a], G.C. Trinchero[b,c],
P. Vallania[b,c], S. Vernetto[b,c], C. Vigorito[c,f]

[a] *Laboratori Nazionali del Gran Sasso, INFN, Assergi (AQ), Italy*
[b] *Istituto di Cosmo-Geofisica del CNR, Torino, Italy*
[c] *Istituto Nazionale di Fisica Nucleare, Torino, Italy*
[d] *Istituto Nazionale di Fisica Nucleare, Bologna, Italy*
[e] *Dipartimento di Fisica dell' Università, L' Aquila, Italy*
[f] *Dipartimento di Fisica Generale dell' Università, Torino, Italy*
[g] *Instituto de Fisica, Universidade Estadual, Campinas, Brazil*
[h] *Dipartimento di Scienze Fisiche dell' Università and INFN, Napoli, Italy*

Abstract

We describe and discuss the operation, calibration and stability of the EAS-TOP calorimeter (Campo Imperatore, National Gran Sasso Laboratories), a large area hadron and muon detector devoted to cosmic-ray physics. It consists of iron slabs (for a total thickness of 818 g cm^{-2}) and Iarocci tubes as sensitive layers, operating in the streamer mode and the "quasi proportional" regime. Using a model describing the operation of the "quasi proportional" chambers, we derive a calibration curve in the energy range 50–5000 GeV, whose reliability has been indirectly checked through on-site measurements, by means of an accelerator beam run (up to $\simeq 600$–700 GeV) and by comparing the model predictions on hadron shower transition curves with the data. © 1999 Elsevier Science B.V. All rights reserved.

* Corresponding author. Tel.: + 39 11 6306810; fax: + 39 11 6604056; e-mail: castellina@to.infn.it.

The aim of the EAS-TOP experiment [1] is to study cosmic rays (energy spectrum, composition, interactions, anisotropies, gamma-ray sources) in the energy range from direct measurements ($\simeq 10^{13}$ eV) to the region *above the knee* of the primary spectrum ($\simeq 10^{16}$ eV). The array is located at Campo Imperatore (2000 m a.s.l.), above the underground Gran Sasso Laboratories, and consists of detectors of the different Extensive Air Shower (EAS) components: electromagnetic [2], muons ($E_\mu > 1$ GeV) and hadrons [3], atmospheric Cherenkov light [4], with the additional possibility of running in coincidence with the muon detectors operating in the underground laboratories ($E_\mu > 1.4$ TeV) [5,6].

The aim of the hadron calorimeter is to study the hadron flux, uncorrelated and in EAS, the energy content and absorption characteristics of the EAS cores and peculiar events (such as the large p_t ones reported in Ref. [7]). Main characteristics of hadron calorimeters for cosmic-ray studies have to be: large collecting areas, large dynamic range (30 GeV–100 TeV in our case), continuity and stability of operation, these beyond the requirements of energy and spatial resolutions as for any high-energy physics detector. Concerning the operation, a main constraint is usually given by the location of such arrays at mountain altitudes and to the non continuous possibility of access in non standard laboratory sites.

A further problem for such detectors (as for usual EAS detectors) is connected to the difficulties of their calibration, in view of the wide energy range required, and therefore involves the presence of possible saturation effects.

Due to the impossibility of a direct calibration of the calorimeter, we followed an approach of *indirect* calibration of the chambers to model the detector response; its discussion is one of the main aims of this paper. The detector (Section 1), the calibration technique (Section 2) and the stability (Appendix) are described. The calibration is based on experimental data obtained both through direct on site measurements (Section 2.1) and by means of a test run performed on a prototype of the detector chambers at a 50 GeV positron beam at CERN (Section 2.2). These data have been used to model the response of the tubes, that has been inserted in a simulation exploiting the GEANT code (Section 3). The energy measurements are discussed in Section 4.

1. The detector

1.1. General description

The EAS-TOP calorimeter is a parallelepiped of $(12 \times 12 \times 3)$ m^3 made of nine identical planes. Each of them is formed by two streamer tube layers for muon tracking, one layer of *quasi proportional* tubes for hadron calorimetry and a 13 cm thick iron absorber, for a total depth of 818 g cm^{-2}, i.e. $\simeq 6.2$ nuclear mean free paths. The detector layout is shown in Fig. 1.

At present, the active layers of the upper plane are unshielded and operate as a fine grain detector of the electromagnetic component of EAS cores. The distance between two successive layers is about 31 cm, except for the 7th and 8th planes, between which $\simeq 24$ cm are left to lodge an additional scintillator layer as a triggering and timing measurement facility at a depth of $\simeq 1.5$ absorption lengths (see Fig. 1b). Two vertical walls (3×12) m^2 are placed at the North and South sides of the calorimeter. Each of them is made of one layer of streamer chambers to improve the detector triggering and tracking capabilities for very inclined muons.

1.2. Mechanics

The calorimeter rests on concrete foundations, made by crisscrossed continuous grade beams, strongly reinforced in order to support both concentrated and distributed loads (up to 70 t/linear meter). The absorber of each plane is given by 92 side-by-side steel billets, each one (130×130) mm^2 in section and $\simeq 12$ m long. The tolerance of the billet length without working is $-0.0/+200$ mm. A single plane weighs $\simeq 150$ t, for a total absorber weight of 1350 t. Due to its great stiffness, each absorber plane is used as bearing plane for the chambers (except for the lowest layer which rests on an ad hoc structure); the supporting frame is given by one central and two lateral beams leaning on the
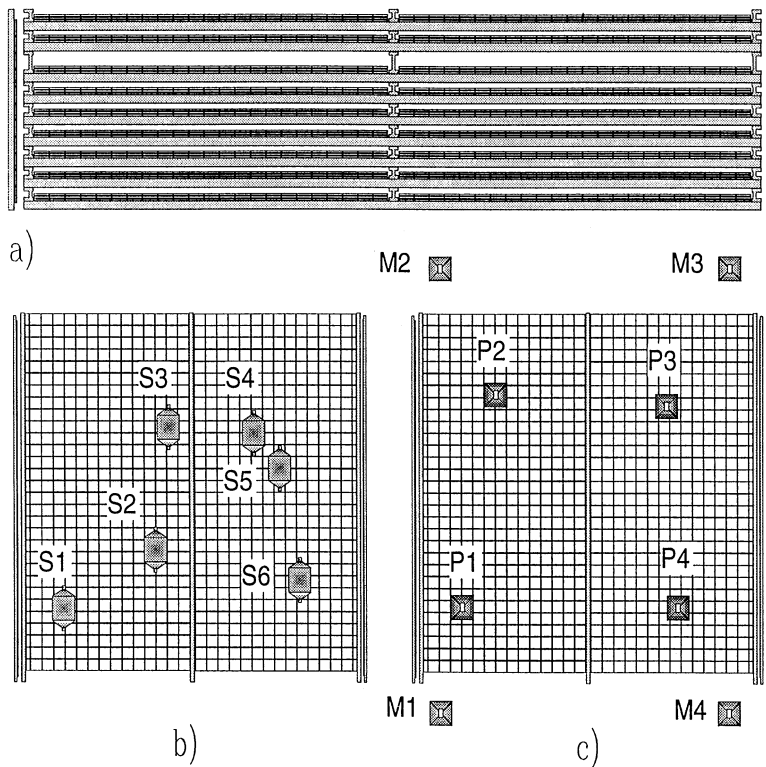
Fig. 1. (a) Layout of the EAS-TOP calorimeter. The frame, the iron absorbers, the three layer chamber structure and the vertical walls are shown; (b) 7th plane, top view, with the S scintillators set; (c) 9th plane, top view, with the M and P scintillators.

underlying billet layer and is constrained to the heads. The central H-beam allows a detector gap in the central line limited to 2 cm, i.e. the thickness of the H-beam web. The whole frame is thus extremely light, equivalent to 2% of the total weight. Horizontal stresses possibly due to seismic movements are averted by means of suitable cross bracings along the four sides of the calorimeter, using steel wire ropes covering $< 12\%$ of the useful space. The detector is thus accessible from each side for maintenance operations. The chambers are parallel to the lateral beams and accessible to the heads for power supply, signal read-out and gas fluxing. The strips (see Section 1.3) exit below the beams (maximum pressure 23 kg/cm^2) to the read out electronics. The gas is distributed in parallel for each half-plane and each chamber layer, flowing

from the sides to the center of each detector plane. Two additional structures, each 12 m long and 3 m high, support vertical detector planes of streamer chambers and strips, on the North and South sides of the calorimeter. In order to access any part of the detector, the supporting structures for the vertical planes are mounted on moving frames sliding on a monorail secured to the base. (Tilting actions are contrasted by suitable guidance given above.)

1.3. The sensitive layers and the electronics

The streamer and quasiproportional tubes [8] consist of 8-cell tubes 12 m long, with (3×3) cm^2 single tube cross section. The tubes are operated with an Argon/Isobutane 50/50 gas mixture

distributed in parallel over the 23 chambers of a half-plane.

● *The streamer tubes.* The two bottom layers of each active plane operate in limited streamer regime, acting as tracking detectors; they use a 100 μm wire and are supplied with HV = 4650 V. The tube walls are coated with graphite (R = 1 KΩ/square) and the whole system is inserted in a PVC container 1.5 mm thick [9]. The two-dimensional read-out is performed using signals from the anode wires (X view) and orthogonal external pick-up strips (Y view), split in two subarrays as shown in Fig. 1, the spacing on both views being 3 cm. Signals (368 X/layer, $352 \times 2Y$/layer) are discriminated locally and the digital information is transferred to the readout electronics. The dead space around the streamer discharge in the present tube design is $\simeq$ 5 mm, thus not allowing studies of high particle densities.

● *The quasi proportional tubes.* The high particle densities (for hadron calorimetry and the study of EAS cores) are recorded with the chambers of the upper layer of each plane that use a reduced wire diameter of 50 μm and operate at voltage HV = 2900 V. These detectors operate in saturated proportional mode with the gain reduced by a factor $\simeq$ 100; the corresponding dead space around the discharge is < 500 μm. The signal charge is picked up by an external (40×38) cm^2 pad matrix placed on top of the detectors; to achieve maximum transparency, the wall resistivity has been increased to 200–700 kΩ/square. The particle density range where the signal charge is proportional to the number of incident particles is thus increased, and we will refer to this detector as a *quasiproportional* one. The pad signals (50 ns rise time) are transferred to the charge integrating ADCs (840 ADC channels/layer) by means of passive chains including a 95 Ω multicoaxial cable 12 m long, a transformer and a 60 m long twisted cable. The 32 channels charge integrating ADC is a multiplexed double 12 bit A/D converter with 15 bit dynamic range [10]. The average gain in the high-resolution region is 0.03 pC/ch, saturation occurring around 1 nC; the total conversion time is 1.6 ms; zero suppression is performed by local processors. The ADC channels are selected on the basis of their linearity characteristics: channels with an integral nonlinearity larger than five channels are rejected.

1.4. The triggers

A set of scintillators is included in the detector for different aims:

● four (80×80) cm^2 scintillator counters (P_1, P_2, P_3, P_4), identical to those of the EAS-TOP electromagnetic detector [2], are placed on top of the 9th plane, at a distance of about 3 m from the calorimeter corners, 5 m from its center (Fig. 1c);

● four other identical scintillators (M_1, M_2, M_3, M_4) are placed outside the detector at the four corners of the 9th plane; together with the P_1–P_4 counters, they are used to select contained EAS cores on the calorimeter surface (Fig. 1c);

● six scintillators of the same dimensions (S_1–S_6) are sitting on the 7th plane for hadronic triggering purposes and timing measurements (Fig. 1b);

● eight (40×38) cm^2 scintillator counters (T_1–T_8), placed on top of the 7th and 9th planes, are arranged to form four telescopes (TEL$_1$–TEL$_4$) to select muons hitting the detector near the input and output of the gas distribution system for monitoring procedures.

The apparatus can be considered as an ensemble of three different detectors which, because of the different time propagations of their signals, have to be independently triggered. They are the tracking detector, the proportional tubes and the scintillator counters. Scintillator counters, which are the fastest devices, are self-triggering and are used to generate the trigger to the whole detector. On the other hand, the tracking detector can retain informations up to 10 μs after the event occurrence and can therefore be triggered by any other detector in the calorimeter and by the EAS-TOP electromagnetic array. The permanently active trigger configurations are:

1. the *external trigger* generated by the EAS-TOP electromagnetic detector, which starts the read out of the tracking detector only (to study the muon component in EAS);

2. the *shower trigger*, provided by the four-fold coincidence of the scintillation detectors (P_1, P_2, P_3, P_4), with the additional condition of at least 200 particles hitting the 9th plane

measured by means of the wire signal of the outer streamer tube layer, which generates the read out of the whole detector (to study the lateral distribution at small core distances and core characteristics);

3. the *hadron trigger*, generated by the logical OR of signals induced in the scintillators (S_1–S_6) located between the 7th and 8th planes, which generates the read out of the whole detector;

4. the *horizonthal trigger*, provided by the coincidence between the two vertical layers and part of the horizonthal layers, which produces the read out of the tracking detector only (to select muons with $\Theta > 70°$).

   Two additional monitoring triggers are active:

5. the *pedestal trigger*, generated every 10 s, which induces the read out of a subset of the proportional detector electronics, where the threshold of the zero suppressing processor is set to 0;

6. the *stability test trigger*, generated by the single particle telescopes (TEL_1–TEL_4). They are enabled to generate a trigger condition inducing the read out of the tracking detector, of part of the proportional counters and of the scintillators.

Finally, additional triggers operate temporarily for short term measurements or calibration purposes.

2. The calibration runs

2.1. The on site runs

On-site runs are performed for the following aims: (a) detector calibration and study of saturation effects; (b) periodical calibrations; (c) study of the experimental fluctuations; (d) systematic checks of the detector stability (see Appendix).

(a) Preliminary runs have been performed to study the saturation of the total induced charge as a function of high voltage and particle arrival direction. A trigger given by the S_1 scintillator on top of the 7th plane together with the tracking reconstruction allows to select single muons at different incident angles on a single pad. The charge spectrum on the pad is then derived, binning the covered angular range (up to 50°) in $\Delta\Theta = 2.5°$ between 0° and 20° and $\Delta\Theta = 5°$ for larger angles. For a proportional counter the induced charge is proportional to the track length; due to the saturated regime, a local lowering of the electric field inside the chamber occurs, not allowing a full development of the cascade. We expect the saturation effects to be relevant when the projection along the wire of the track length inside the tube is small. The dependence of the average induced charge $\langle Q \rangle$ on the cosine of the projected zenithal angles on the two views is shown in Fig. 2 for three different applied voltages. The effect is clearly seen and – as expected – it appears smaller at lower HV regime. We choose to operate at HV = 2900 V as a compromise between reducing this effect and having a clear single particle signal on the ADCs. The saturation region corresponds to tracks with $\vartheta_y \leq 15°$ (along the wires). No saturation effect is seen for incidence perpendicular to the tubes.

(b) The in situ response is periodically checked in devoted calibration runs. A *single muon trigger* is obtained by means of the AND of the discriminated analogic signal of the streamer chambers (eight tubes), respectively, below the 2nd and the 8th level of proportional tubes. The trigger rate is about 40 Hz. The calibration runs can be remotely controlled, not requiring on-site technical assistance. The muon arrival direction and the impact position on each layer are obtained from the track reconstruction [11] with an accuracy < 0.5 cm. By means of this procedure, we get for each pad the mean charge induced by a single ionizing particle and the inefficiency, that is the probability of a signal compatible with the ADC pedestal fluctuations, even for particles crossing the pad (the geometric inefficiency alone is $\simeq 8\%$).

The procedure is the following:

• Derivation of the charge spectrum q^α, defined as

$$q^\alpha = q \times \cos \vartheta_y \tag{1}$$

independent from the particle direction (according to Fig. 2). To avoid saturation effects, the q^α spectrum is evaluated only for tracks with $15° \leq \vartheta_y \leq 50°$. Examples of charge distributions of q and q^α are shown in Fig. 3a and c, respectively.
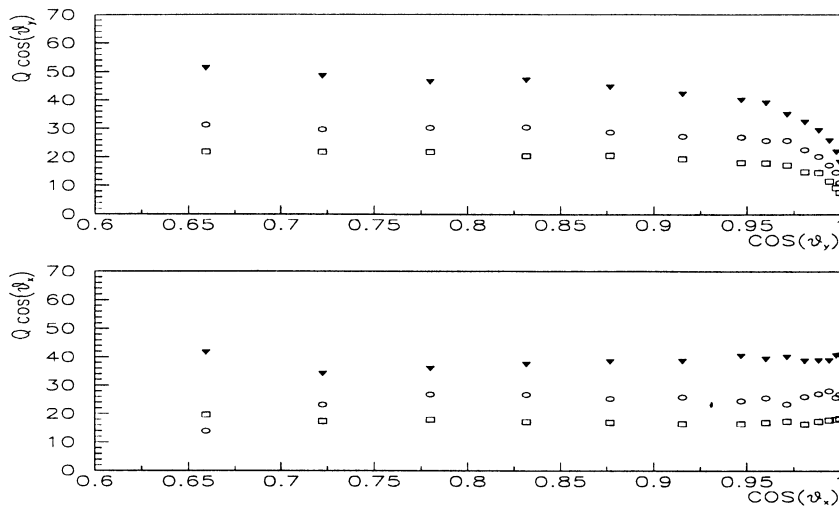
Fig. 2. Average charge induced by single muons on the pad, corrected for the cosine of the incident zenithal angle, as a function of the cosine of the projected angles θ_x (perpendicular to the wires) and θ_y (along the wires) for different applied high voltage. Full triangles: HV = 3000 V, empty circles: HV = 2950 V, empty squares: HV = 2900 V.
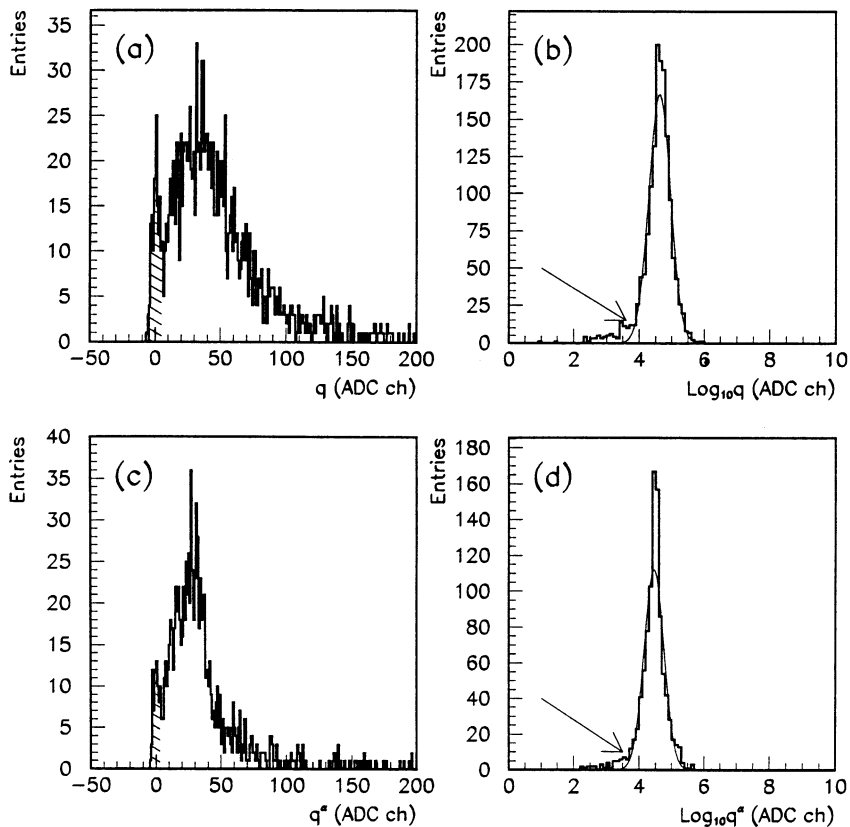

Fig. 3. Charge distribution q (a) and the same distribution as a function of the logarithm of q (b) (with Gaussian fit superimposed). The shadowed area (a) shows the inefficiency region, determined as the one to the left of the arrow in (b). (c) and (d) show the same distributions for q^z.

● Such charge spectra are with good approximation log-normal and in order to easily analyze the spectra and determine the inefficiency of the pad, we derive the log q^{α} distributions, which actually result quite well described by Gaussian distributions (see Fig. 3b and d).

● A fit with a Gaussian distribution is performed on the log q spectra, thus identifying the pad inefficiency ε. The mean value is finally recalculated, excluding such inefficiency region. The fit to the log q and log q^{α} distributions and the determined inefficiency regions are also shown in Fig. 3. The average charge $q^{\alpha}_{\mathrm{eff}}$ and the inefficiency ε thus estimated for each pad are stored in a calibration file for further use. The average value of $q^{\alpha}_{\mathrm{eff}}$ is about 0.82 pC/particle, ε is around 12%. The number of pads actually used in the analysis is greater than 96%. The charge (Q_{ADC}) induced on the pad is converted to the number of equivalent particles N with the expression

$$N = \frac{Q_{\mathrm{ADC}}}{q^{\alpha}_{\mathrm{eff}} + \kappa(X - X_{\mathrm{Cal}})} \cdot \frac{1}{1 - \varepsilon}, \tag{2}$$

where X_{Cal} is the value of the ratio $X = p/T$ at the calibration epoch, when the calibration constant $q^{\alpha}_{\mathrm{eff}}$ is measured (p and T being constantly recorded). For the value of the constant κ, see the Appendix. The accuracy in the average charge evaluation is $\simeq 3\%$ of the absolute value.

(c) The information on the fluctuations in response to different particle densities has been obtained during data taking, in order to take into account the experimental conditions. Concerning single particles, e.g. Fig. 3c, we get for the whole detector a value of $\sigma/\langle q^{\alpha}\rangle = 0.97$ for vertical muons. For large particle densities, the fluctuations have been measured with two different methods: (i) by comparing the ADC counts (number of *equivalent particles*) measured by a pad with the pulse height of a T_i scintillator positioned on top of the pad itself; (ii) by studying the fluctuations of the ADC counts for a pad compared to the average value of the eight nearby ones. The results of the two techniques are compared in Fig. 4, the different Poissonian fluctuations for case (ii) being corrected for. Also shown is the best fit obtained
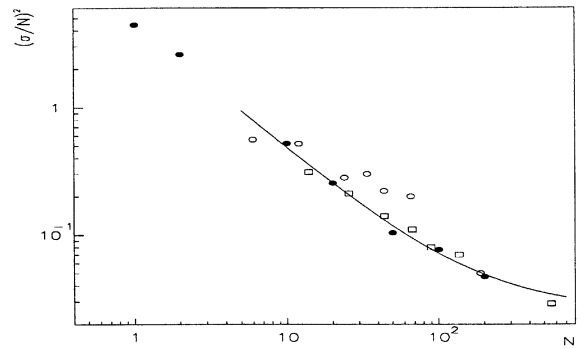

Fig. 4. Fluctuations of the pad response. (○) experimental data (i); (□) experimental data (ii); line: expression 3, see text; (●) Monte Carlo simulation results described in Section 3.1.

with expression

$$\left(\frac{\sigma}{N}\right)^2 = a^2 + \frac{b^2}{N}, \tag{3}$$

where $a = 0.16$ and $b = 2.15$. Term "a" accounts mainly for systematic uncertainties, due to pad inefficiencies and instabilities in the gas distribution; term "b", beside taking into account the Poissonian fluctuations, is connected with geometrical effects which increase the statistical fluctuations.

2.2. The beam run

A test run has been performed at the 50 GeV e^+ beam at CERN, with the aim of:

1. calibrating the chamber response to large particle densities, using a lead target 4 cm thick ($\simeq 7$ radiation lengths) in order to have maximum particle density inside a single tube;
2. checking the response to HE e.m. cascades developing in iron, which is the calorimeter absorber;
3. comparing the experimental results with a simulation including the modeling of the tube response to large particle densities.

The detector was built by chambers with the same characteristics and similar gas mixture as the ones operating on site, but with reduced length

(1.2 m), seen by three pads. The power supply was fixed at 3200 V, to reproduce the same signals (i.e. the same collected charge) at sea level (atmospheric depth 1000 g cm^{-2}) as at the site of the experiment (810 g cm^{-2}). The beam, of dimension (3×3) cm^2, was centered 2 cm away from the center of the pad. About 90% of the signal was collected. The chambers were calibrated with single muons, following a procedure similar to the one described in Section 2.1b, but integrating over the angular distribution. Results will therefore be given in terms of number of equivalent particles N (averaged over their angular distribution) recorded in the calibration run. The stability during the run was checked using the signals from a 22 keV Cd source positioned on a pad not directly exposed to the beam. Three different measurements have been performed and the experimental results are shown in Fig. 5 together with the expectations from the simulation of the chambers' response (see Section 3.2).

Different particle densities obtained through different primary energies E_0, with the lead target positioned at different distances d from the chamber, have been explored. The response as a function of energy (from 2 to 50 GeV, $d = 12$ cm) is plotted in Fig. 5a. The data obtained at fixed primary energy (50 GeV) and different distances from the absorber ($d = 0$–16 cm) are shown in Fig. 5b. The beginning of saturation in the chambers is observed above particle densities corresponding to $\simeq 30$ GeV in Fig. 5a and for small air gaps in Fig. 5b. The decreasing values of N at large distances is due to geometry. The measured longitudinal development of the cascade at $E_0 = 50$ GeV is shown in Fig. 5c in steps of 0.5 cm (thickness x of the iron absorber).

3. Modelling the response of the quasi proportional tubes

3.1. The model

The response of the calorimeter to single muons, electromagnetic and hadronic showers has been studied by means of a full Monte Carlo simulation based on the Geant 3.21 code [12] reproducing the cascades in the calorimeter, where a complete description of the geometry, as described in Section 1, has been included. The hadronic processes have been simulated using the Fluka code. The response of the quasi proportional tubes discussed in the following has been included in the Geant code. The behavior of the quasiproportional tubes has been modeled by considering the ionization density produced by a charged particle. In the gas filling the tubes, Ar and isobutane in proportion $50 + 50$, $K = dq/dl = 145\,e^-$ ion pair/cm are produced on average; the total ionization is given by KL, where L is the total track length of the crossing particle in the single tube. If d_{diff} is the electron diffusion length in the gas, the local linear charge density on the wire will be

$$\delta = \frac{KL}{\sqrt{\Delta y^2 + d_{\mathrm{diff}}^2}} = \frac{KL}{\Delta y^*}, \tag{4}$$

where Δy is the projection of L along the wire. We then define $x = \delta/K$ the local charge density normalized to the one of a minimum ionizing particle; x is obviously maximum for tracks orthogonal to the chamber, i.e. for $\Delta y = 0$, $x_{\max} = L/d_{\mathrm{diff}}$. The
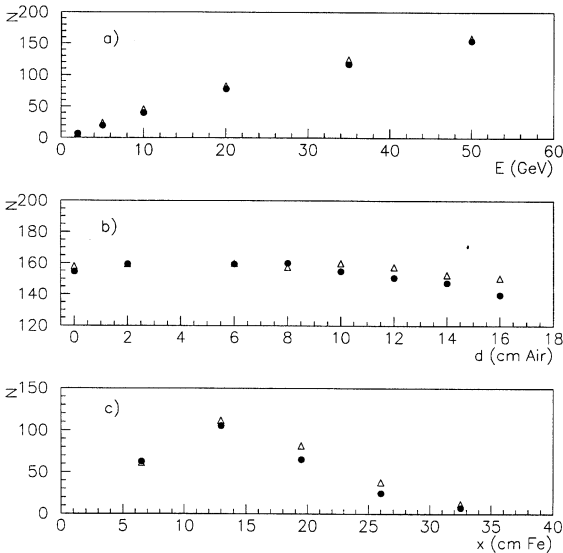

Fig. 5. Comparison between the test beam measurements (empty triangles) and the Monte Carlo simulation (full circles). (a–c, see text).

charge Q in the tube is the product of the total ionization and a function of the local charge density

$$Q = A(\delta)KL = A_0 f(\delta)KL, \qquad (5)$$

where $A_0 K$ is the asymptotic value $(Q/L)_{\text{norm}}$ for $f(\delta) = 1$. Finally

$$\frac{Q/L}{(Q/L)_{\text{norm}}} = f(\delta). \qquad (6)$$

In order to obtain an experimental measurement of the function $f(\delta)$, the data from the run described in Section 2.1a are used. Calculating the effective track length in the tube and its projection on the wire for each reconstructed muon, the above defined function $f(\delta)$ can be obtained; its behavior as a function of x is shown in Fig. 6 for HV = 2900 V and diffusion $d_{\text{diff}} = 0.1$ cm.

The ionization density in case of many particles on the same tube has been reproduced by summing the contributions of all the track lengths corresponding to the same portion of wire. For example, let us consider two particles crossing a tube with track lengths L_1 and L_2, respectively. If in the same Δy they contribute with L_1' and L_2', their total ionization density in such a portion of wire will be

$K(L_1' + L_2')/\Delta y^*$, so that

$$Q = A_0 f(\delta) K(L_1' + L_2'). \qquad (7)$$

The induced charge picked up by the pad is given by

$$Q_{\text{ind}} = C \frac{Qd}{2\pi} \iint \frac{1}{(d^2 + x^2 + y^2)^{1.5}} \, dx \, dy, \qquad (8)$$

where x and y are the spatial coordinates on the pad relative to the position of the inducing charge in the tube and $d = 1.5$ cm is the distance between the wire and the pad. The normalization C is such that 37% of the charge localized in the tube in correspondence of the pad center is collected by the external cathode, according to the results obtained on test tubes after optimization of their characteristics to allow for maximum transparency. Furthermore, it can be shown that: (i) for a charge Q_{ind} induced in the center of the pad, the induction on the adjacent pads reduces to $\simeq 0.05 \, Q_{\text{ind}}$. This behavior is shown in Fig. 7 as a function of the distance r from the pad center; (ii) the induced charge integrated on the crossed pad reduces from $\simeq 37\%$ for a particle in the center (sum of the first 5 bins in Fig. 7) to $\simeq 19\%$ for a particle at the corner of the same pad. In order to build a reliable
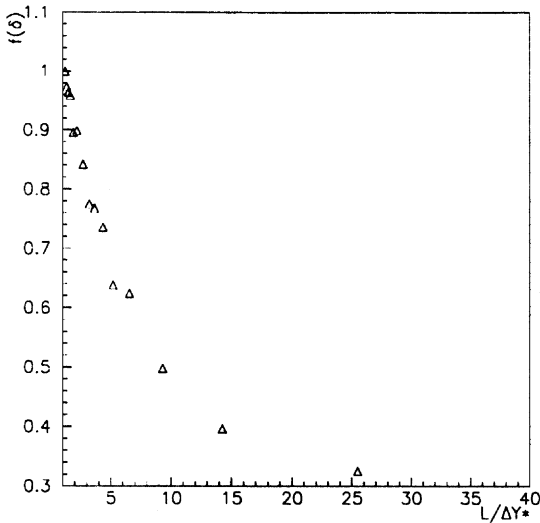

Fig. 6. Normalized charge density as a function of $x = L/\Delta y^*$ for $d_{\text{diff}} = 0.1$ cm, HV = 2900 V.
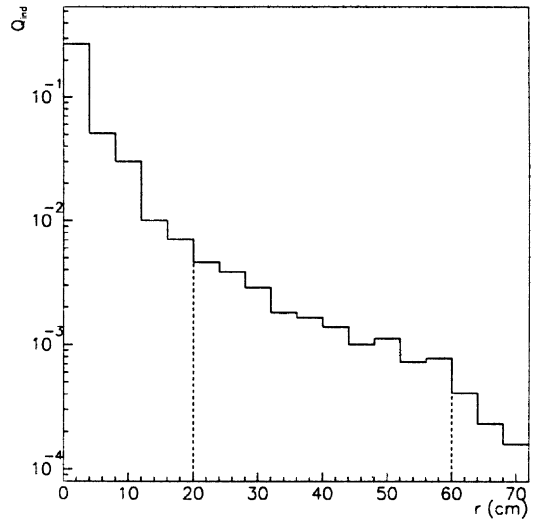

Fig. 7. Average charge $\langle Q_{\text{ind}} \rangle$ induced by a particle crossing the pad center vs. r. Dashed line: pad border.

description of the calorimeter response, it is of major importance to know the fluctuations in the collected charge. The following sources of fluctuations have been included in the simulation:

- fluctuations in the ionization energy losses inside the proportional tube, following the Landau theory;
- fluctuations of the induced charge from individual particles, described in Section 2.1b;
- additional instrumental fluctuations. A 16% term has been added to agree with the measured dispersions (see Section 2.1c, Fig. 4).

In Fig. 8, the simulated single particle response distribution is shown. The experimental width ($\simeq 85\%$) and inefficiency ($\simeq 12\%$) are well reproduced (see Section 2.1).

3.2. The response to electromagnetic showers

As regards large particle densities, the simulation code has been tested by comparing the response to simulated electromagnetic showers to the one obtained at the CERN e^+ beam test described in Section 2.2. The three experimental measurements of Fig. 5(a–c) have been reproduced.

- Fig. 5a: Response to positrons of energies 2–50 GeV; the simulated and measured values show a percentage difference $\leq 2\%$. The simulation of the chamber response is thus tested up to a particle density of $\simeq 300$ particles/cm^2, corresponding to a 50 GeV electromagnetic shower after 4 cm lead absorber; the same particle density, for iron absorber and the calorimeter geometry, corresponds to $\simeq 600$–700 GeV hadrons, which is therefore the effective energy up to which the model is tested.
- Fig. 5b: Simulation results for 50 GeV e^+ as a function of the air gap between the pad and the absorber; the agreement with the experimental data is quite good. In particular, it is excellently close to the absorber, thus confirming the reliability of the model describing the behavior of the proportional tube at the highest particle densities.
- Fig. 5c: Comparison between the experimental and the simulated transition curves in iron: a $\simeq 5\%$ difference is found in correspondence of the shower maximum. The resulting total systematic uncertainty, obtained from the integration of the transition curve, is $\simeq 10\%$.

4. Hadron energy measurement

As an example, we discuss the calibration and resolution in the measurement of single hadron energies. Physical events are selected according to the following trigger: a signal (≥ 20 particles) from
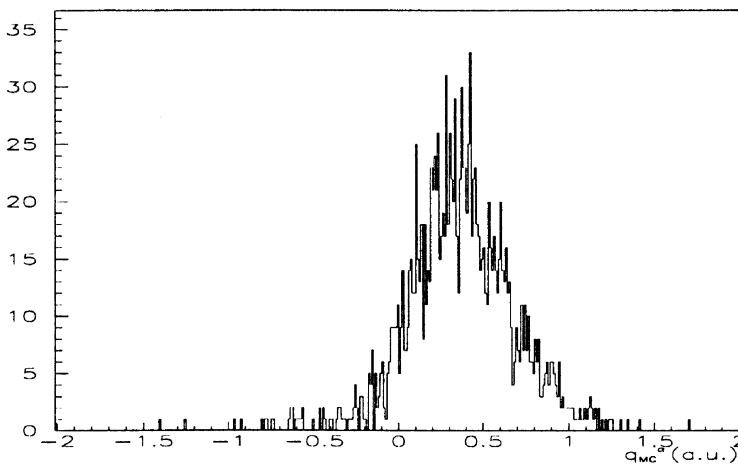

Fig. 8. Response distribution for a single particle in a pad.

one among the six scintillators (S_1–S_6) sitting on top of the 7th plane of the calorimeter and at least 3 planes with maximum induced signal on the pads belonging to the same column, over an area of ($3 \times 3 \times 9$) pads centered on the triggering scintillator. Individual hadrons are further selected by requiring ≤ 100 reconstructed particles on the top layer. In such a configuration, the trigger efficiency for $E = 1000$ GeV protons runs from 100% in the vertical direction to 14% at $\theta = 30°$; at $E = 100$ GeV, from 82% to 12%, respectively. A complete set of Monte Carlo simulations has been run at fixed primary energies in the range 30–5000 GeV, requiring the same trigger configuration; the input angular distribution is the one calculated for residual protons at the experimental depth ($\langle \theta \rangle \simeq 22°$). The chamber response model described in Section 3.1 has been included; the reconstruction procedures are the same as for experimental data. The resulting calibration curve is shown in Fig. 9 and is well described by the expression

$$E = (0.16\ 10^{-4}\ N^2 + 0.37N + 7.96), \qquad (9)$$

including therefore nonlinear effects.

The energy resolution is shown in Fig. 10. The best fit to the resolution is given by

$$\left(\frac{\sigma e}{E}\right)^2 = \left(0.09 + \frac{1.08}{\sqrt{E}}\right)^2 + (0.04\sqrt{E/L_{95\%}})^2, \quad (10)$$
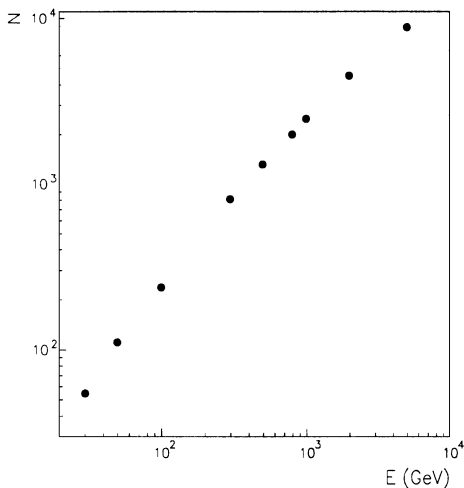
where $L_{95\%} \simeq (9 \ln E + 40)$ cm for iron (E in GeV) [15]. It amounts to $\simeq 15\%$ at 1000 GeV, deteriorating to $\simeq 40\%$ at 30 GeV due to the sampling and to 25% at 5000 GeV due to leakage losses; the total depth of the calorimeter ($\simeq 6.2\lambda_I$) in fact ensures a good shower containment up to $\simeq 1$ TeV. These results are inside the expectations for calorimeters based on iron absorber and such sampling depths [16].

As discussed, the model is tested up to particle densities corresponding to $\simeq 600$–700 GeV. In the TeV region, where no direct check is feasible, a comparison has been made between the experimental and the simulated transition curves for hadron showers. This is shown in Fig. 11, for hadron energies ranging from 0.5 to 5 TeV (according to expression 9 and Fig. 9). Of particular interest are the points corresponding to the highest particle densities, i.e. near the maximum of the shower development at 5 TeV, where the agreement between simulation and experimental data is within $\simeq 10\%$. This shows that the saturation effects are well described by the chamber response model at least up to 5 TeV.

Fig. 9. Total number of particles induced in the calorimeter as a function of the primary proton energy.
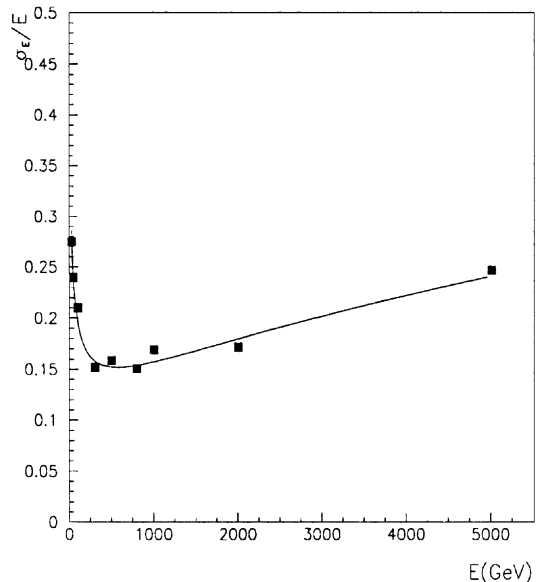

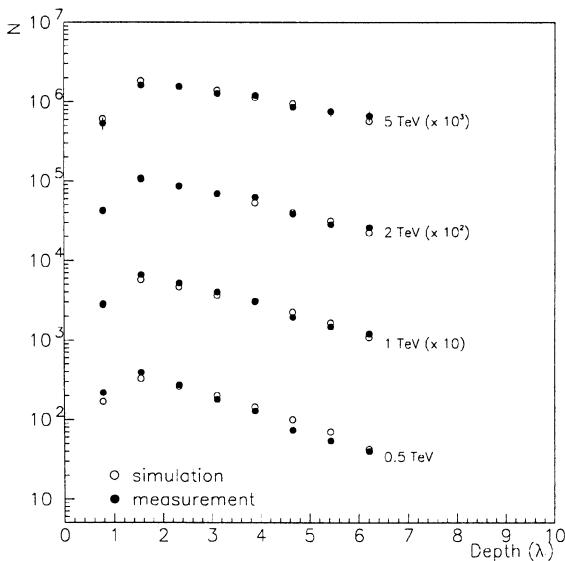Fig. 10. Energy resolution. The best fit according to Experiment 10 is also shown.

Fig. 11. Mean longitudinal transition curves for hadrons. Full circles: data; empty circles: simulation.

5. Conclusions

The operation and calibration of the EAS-TOP calorimeter are discussed. A model describing the operation of quasiproportional tubes has been elaborated and tuned according to the on-site calibration data and to the results of a test run performed at a positron beam at CERN. A calibration curve is derived in the range 30–5000 GeV; the energy resolution is $\simeq 15\%$ at 1 TeV and $\simeq 25\%$ at 5 TeV. Systematic uncertainties on the overall calibration amount to $\simeq 10\%$. The upper limit to the maximum variations due to long-term instabilities is within 16%.

The response of the detector is calibrated in particle densities through the e^+ run up to $\simeq 600$–700 GeV hadron energy. The agreement of the experimental and simulated transition curves for single hadrons extend such energy range, with the same reliability, up to $\simeq 5$ TeV. First results on the hadron spectrum at the atmospheric depth of 810 g cm^{-2} and on the energy content of the EAS cores have been presented in Refs. [17,18].

Appendix A. The on-site stability checks

A.1. Electronics and noise

The continuous monitoring of the ADC pedestals is performed by generating asynchronous gates to the A/D converters of reference channels (one every 30 s). This, besides providing a check of the electronics stability during data taking, provides a measurement of the noise of the system. The distribution of the root-mean-square values of the pedestal spectrum for all the 840×9 channels is shown in Fig. 12. The average noise results to be less than 5 ADC channels, to be compared to a value of 30 ADC channels for the single particle.

A.2. Stability

The detector stability is monitored on-line through cosmic-ray muons selected by means of the scintillator triggers described in Section 1. For each telescope (TEL$_i$) the trigger condition provided by the two scintillators together with the reconstruction from the tracking system allows the acquisition of 400 single muons/h on the 9th layer with $\theta < 27°$ and 50 ev/h with $\theta < 8°$ on the first layer. The pad charge spectra are corrected for the pad inefficiency. The aims of the measurement are: (i) to study the dependence of the average collected charge per single incident particle (single particle response, SPR) on the pressure and temperature conditions [13,14]; (ii) to monitor the detector stability concerning both the gas mixture and long-term systematic variations; (iii) to correct the response for systematic variations between different calibration runs.

(i) The expected inverse proportionality of the signal with respect to the gas density, given by the quantity $X = P/T$, has been checked by studying

the experimental relation

$$\frac{Q - \bar{Q}}{\bar{Q}} = k \cdot \frac{X - \bar{X}}{\bar{X}} + \delta_{\text{gas}}, \qquad (11)$$
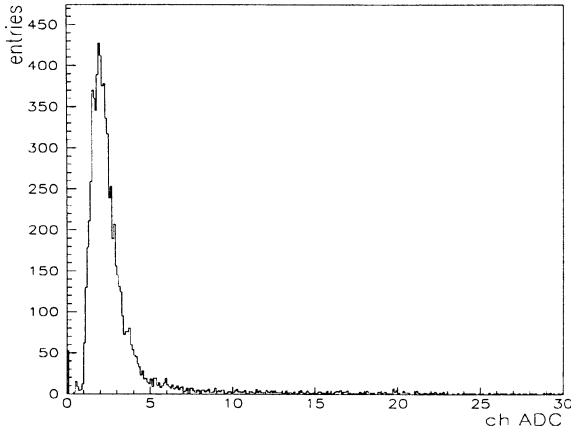

Fig. 12. Distribution of the root-mean-square values of the pedestal spectrum for all channels.

where δ_{gas} takes into account possible instabilities in the gas mixture. We report the analysis performed over $\simeq 1$ yr of data taking; a regression coefficient k has been obtained for each month for the pads of the highest layers (6th–9th, providing the best statistics). An example of the $Q(X)$ monthly correlation is shown in Fig. 13 for the three pads of the 6th–8th layers. The expected behavior is well reproduced, with slightly different values of k among the different pads. The obtained average value $k = (-39 \pm 5)$ ch/(mb/K), i.e. $k = (-1.5 \pm 0.2)$ part/(mb/K), using the average SPR, is currently used during the analysis to correct the data; the errors represent the scatter of the values obtained in different runs for different pads.

(ii) The position of the telescopes (TEL_1–TEL_4) in the module, at the input and at the center of the gas distribution line is such as to allow a systematic check of the gas mixture stability. An example of an anomalous episode, observed during the setting up of the detector, and connected to an unbalance of
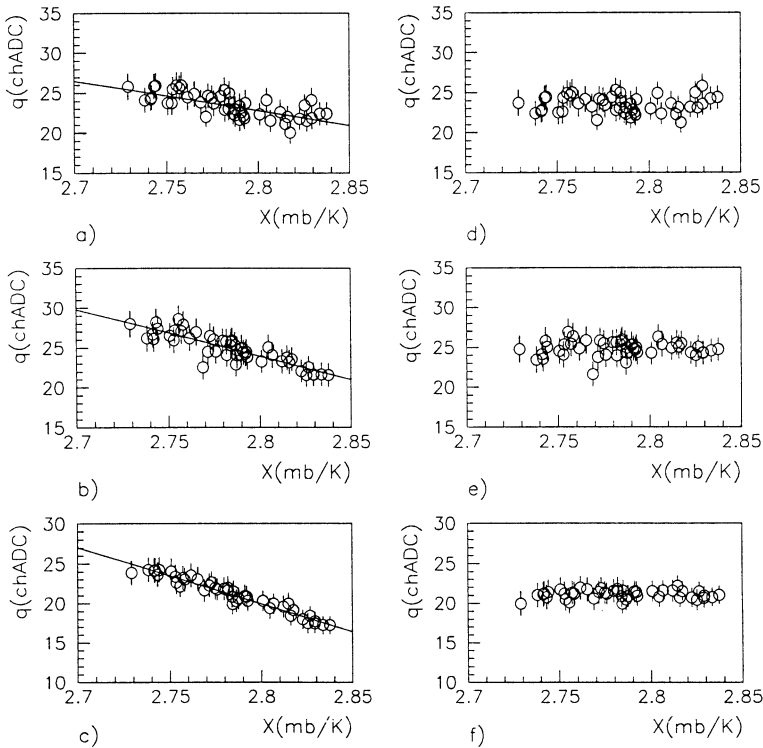

Fig. 13. $Q(X)$ monthly correlation vs X (mb/K) before (leftmost) and after (rightmost) correction. The line shows the best fit to the data according to Eq. (11) (a, d) layer 6; (b, e) layer 7; (c, f) layer 8.
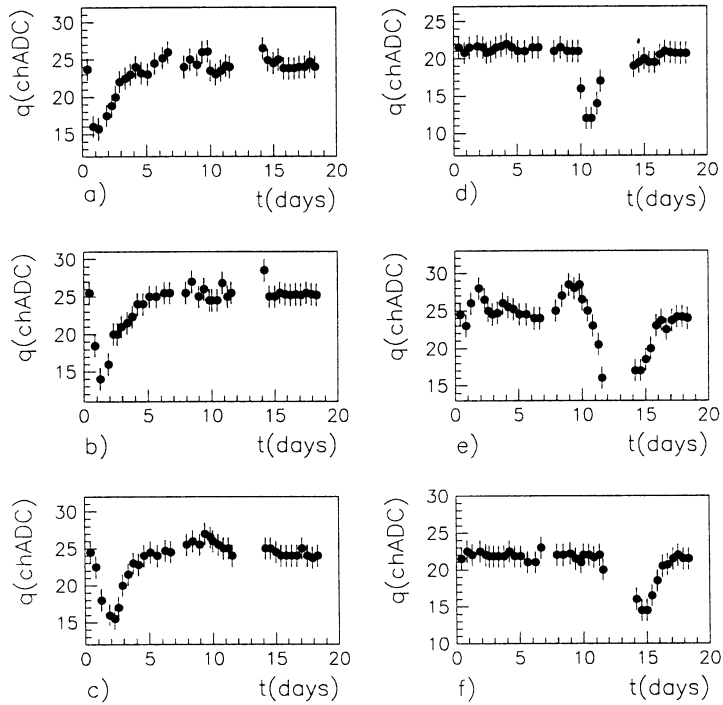
Fig. 14. Single particle response vs. time for layers 6–8. The input (left) and center (right) of the gas distribution line are shown.
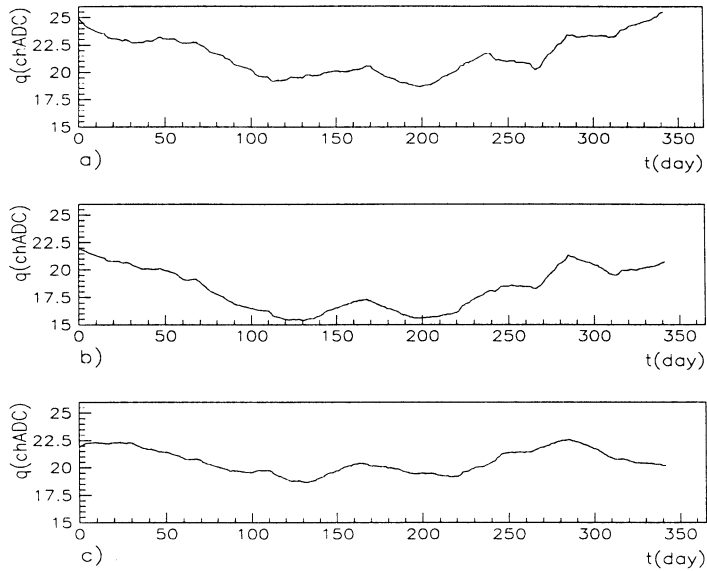

Fig. 15. Single particle response during one year of data taking for layer 6. (a) input and (b) central pads; (c) same as (b) but corrected by means of the input one.

the gas mixture, is shown in Fig. 14, where the SPR is shown for the 6th–8th layer pads localized at the input and at the center of the gas distribution. The same decrease in the response observed at the gas distribution input is observed at the center with a delay of about 10 days, which is the approximate crossing time of the gas along the chamber lines. An on-line program alerts the user in case of variations larger than 15% in the response on several layers.

(iii) Fig. 15 shows the behavior of the SPR during the year of data taking used in the present analysis for the input and central pads of the 6th layer (Fig. 15a and b, respectively). The behaviour of the two responses is similar. Such correlation is verified on all layers, thus showing the presence of systematic effects, even if slightly different, on each layer. The SPR data for the central pads on layer 6, shown in Fig. 15b, corrected with the data of Fig. 15a, are shown in Fig. 15c, systematic trends being strongly smoothed, the residual maximum variation being $\sim 16\%$. EAS data are corrected in the same way, by using the mean value of the responses of the input and central pads: thus, the quoted 16% represents the upper limit to uncorrected long-term instabilities.

References

[1] M. Aglietta et al., (EAS-TOP Collaboration), Il Nuovo Cimento 9C (1986) 262.

[2] M. Aglietta et al., (EAS-TOP Collaboration), Nucl. Instr. and Meth. A 336 (1993) 310.

[3] M. Aglietta et al., (EAS-TOP Collaboration), Il Nuovo Cimento 15C (1992) 735.

[4] M. Aglietta et al., (EAS-TOP Collaboration), Il Nuovo Cimento 15C (1992) 357.

[5] R. Bellotti et al., (MACRO and EAS-TOP Collaborations), Phys. Rev. D 42 (1990) 1396.

[6] M. Aglietta et al., (EAS-TOP and LVD Collaborations), Il Nuovo Cimento 105A (1992) 1815.

[7] M. Aglietta et al., (EAS-TOP Collaboration), Il Nuovo Cimento 18C (1995) 663.

[8] G. Battistoni et al., Nucl. Instr. and Meth. A 176 (1980) 297.

[9] M. Anelli et al., Nucl. Instr. and Meth. A 289 (1990) 294.

[10] F. Burgeois, A. Corre, J.B. Marcelin, A. Meyrier, G. Schuler, IEEE Trans. Nucl. Sci. NS-34 (1981) 240.

[11] M. Aglietta et al., (EAS-TOP Collaboration), Proc. XXIII ICRC, 4, Calgary, 1993, p. 251.

[12] Application Software Group and Network Division, GEANT: Detector description and Simulation tool 3.21, CERN W5013, 1994.

[13] A. Messineo et al., Nucl. Instr. and Meth. A 320 (1992) 177.

[14] M. Aglietta et al., (EAS-TOP Collaboration), Proc. XXIII ICRC, 4, Calgary, 1993, p. 692.

[15] Prokoshkin Yu.D., Proc. of the II ICFA Workshop on Possibilities and Limitations of Accelerators and Detectors, Les Diablerets, U. Amaldi Ed., CERN, 1980, 405.

[16] U. Amaldi, Physica Scripta 23 (1981) 409.

[17] M. Aglietta et al., (EAS-TOP Collaboration), Proc. XXV ICRC, 6, Durban, 1997, p. 81.

[18] M. Aglietta et al., (EAS-TOP Collaboration), Proc. XXV ICRC, 6, Durban, 1997, p. 161.